

## Shape reconstruction of subcellular structures from live cell fluorescence microscopy images

J.A. Helmuth<sup>a,\*</sup>, C.J. Burckhardt<sup>b</sup>, U.F. Greber<sup>b</sup>, I.F. Sbalzarini<sup>a,\*</sup>

<sup>a</sup>Institute of Computational Science and Swiss Institute of Bioinformatics, ETH Zurich, CAB G34, CH-8092 Zurich, Switzerland

<sup>b</sup>Institute of Zoology, University of Zürich, Winterthurerstr. 190, CH-8057 Zurich, Switzerland

### ARTICLE INFO

#### Article history:

Received 2 October 2008

Received in revised form 30 March 2009

Accepted 31 March 2009

Available online 7 April 2009

#### Keywords:

Virus entry  
Endosomal trafficking  
Image analysis  
Shape reconstruction  
Deconvolution

### ABSTRACT

Live imaging of subcellular structures is indispensable to advance our understanding of cellular processes. The blurred digital images acquired in light microscopy are, however, complex to analyze, and identification and reconstruction of subcellular structures from such images remains a major challenge. We present a novel, model-based image analysis algorithm to reconstruct outlines of subcellular structures using a sub-pixel representation. The algorithm explicitly accounts for the optical properties of the microscope. We validate the reconstruction performance on synthetic data and apply the new method to fluorescence microscopy images of endosomes identified by the GTPase EGFP-Rab5. The benefits of the new algorithm are outlined by comparison to standard techniques. We demonstrate that the new algorithm leads to better discrimination between different endosomal virus entry pathways and to more robust, accurate, and self-consistent quantification of endosome shape features. This allows establishing a set of features that quantify endosome morphology and robustly capture the dynamics of endosome fusion.

© 2009 Elsevier Inc. All rights reserved.

### 1. Introduction

A central paradigm in structural cell biology is that the microscopic shape of subcellular objects is closely linked to their function. Shapes that result from dynamic processes can be used as indirect process readouts (Neumann et al., 2006), while shapes can also determine or constrain a biological function (Sbalzarini et al., 2005). Correlating the positions and shapes of populations of different objects allows mapping cellular organization (Nickell et al., 2006) and investigating specific interactions amongst them. Extracting shape information from live cells is, therefore, of great interest. Advances in light microscopy (Stephens and Allan, 2003) and the development of fluorescent tags for specific labeling of proteins (Giepmans et al., 2006) have rendered fluorescence light microscopy the most widely used experimental tool for imaging subcellular structures in vivo. The acquired images contain a wealth of information, which is, however, complex and under-explored, and requires reduction to a comprehensible form. The development of computational image processing tools that extract the biologically relevant information has, therefore, attracted great attention. Diverse tasks have been addressed, ranging from histogram analysis and computation of spatial intensity moments to

complex image analysis such as segmentation, pattern recognition, or the integration of temporal information in object tracking. Simple shape models for point-like structures such as viruses or vesicles (Cheezum et al., 2001; Sbalzarini and Koumoutsakos, 2005), linear structures such as cytoskeletal elements (Danuser and Stricker, 1998), or structures with a Gaussian intensity distribution (Li et al., 2004; Rink et al., 2005) are widely used. More complex models have been developed to analyze, e.g., cell boundary movements (Machacek and Danuser, 2006) or chromosome segregation patterns (Neumann et al., 2006).

Two approaches to extracting shape information from images can be distinguished: (1) Pixel-based methods extract information directly from the images. Image transformations are applied to highlight features of interest such as edges or peaks of intensity. In a post-processing step, object descriptions can be constructed from the image features. These methods rely on the implicit assumption of a one-to-one correspondence between the features of the image and the true object. (2) Model-based methods explain the image in a bottom-up approach using (physical) object and imaging models. These methods rely on strong prior knowledge about the shape of the imaged objects. Such prior knowledge increases the detection power, but decreases the explorative power of image analysis methods.

The size and shape of the objects of interest determine when a more elaborate model-based approach is favorable: In standard far-field fluorescence microscopy, only objects larger than the wavelength of light can be resolved (Stephens and Allan, 2003;

\* Corresponding authors.

E-mail addresses: [jo.helmuth@inf.ethz.ch](mailto:jo.helmuth@inf.ethz.ch) (J.A. Helmuth), [ivos@ethz.ch](mailto:ivos@ethz.ch) (I.F. Sbalzarini).

Hell, 2007). Images of individual point sources have the shape of a Mexican hat. In the visible spectrum, the diameter of this so-called point spread function (PSF) is between 200 and 500 nanometers (nm). As a consequence, many small subcellular structures appear heavily blurred in light microscopy images and the apparent width of their boundary is comparable to their size. Pixel-based boundary localization methods, such as methods based on edge strength, can therefore be significantly biased because the implicit assumption that the local maxima of an edge strength function coincide with the true object boundary is not necessarily true.

Here, we provide a robust methodology to quantitatively analyze the morphology of complex-shaped subcellular objects in live cells imaged by fluorescence microscopy. Our model-based algorithm overcomes limitations of classical pixel-based approaches by explicitly accounting for the physics of the imaging equipment and combining a flexible shape model with concepts from deconvolution. We demonstrate the development of a specific object shape model for endosomes. We then benchmark the performance of the algorithm on synthetic test images, and use it to reconstruct outlines of Rab5-positive endosomes in live cells in the context of sorting processes and virus infection.

Endosomes are dynamic lipid-bounded organelles that are formed by invaginations of the plasma membrane (Mellman and Warren, 2000). The size of endosomes is in the order of 20 to several hundred nanometers, they are unevenly distributed in the cytoplasm, and the number of objects per unit volume is high. The complexity of endosomal shapes has been demonstrated using cryo-electron microscopy and tomographic reconstruction in fixed samples at high spatial resolution (Hayashi et al., 2008). In live cells, however, the static and dynamic morphology of endosomes has not been characterized so far, partly due to difficulties pertaining to acquiring and analyzing images of such small objects.

Our results show that the highly accurate sub-pixel-resolution outlines reconstructed by the present method enable morphometric analyses of endosomes or similarly small intracellular structures. The results of such analyses are superior to those found by classical pixel-based image segmentation, enabling better discrimination between different experimental conditions. We exemplify these benefits in three case studies, quantifying and analyzing endosome shapes and distributions during endosome fusion and sorting of two endosomal viruses.

## 2. Outline reconstruction algorithm

We reconstruct the outlines of subcellular objects from noisy digital fluorescence microscopy images using a sub-pixel representation. This reconstruction is based on models of the imaging process and the imaged object and estimation of object shape model parameters. Nevertheless, careful preprocessing and segmentation of the images is performed in order to render the estimation procedure robust and efficient.

The model of the imaging process (Fig. 2D–F) starts from a function  $O(x, y)$ , representing the actual concentration of fluorophores on the object at each point in the focal plane. In a digital image, this amounts to attributing each pixel  $(x_i, y_j)$  a fluorescence level  $O(i, j)$  through the so-called *object intensity function* (Fig. 2D). Image formation in the microscope is modeled as a convolution of the object intensity function  $O$  with the (measured) PSF  $P$  of the light microscope. This yields the noise-free image (Fig. 2E)

$$I = O * P, \quad (1)$$

where  $*$  denotes the mathematical operation of convolution. In any real imaging system, the measurements are corrupted by noise  $E(i, j)$ , yielding an observed image (Fig. 2F)  $I_m(i, j) = I(i, j) + E(i, j)$ .

Reconstructing  $O(i, j)$  directly from an observed image  $I_m(i, j)$  constitutes a classical deconvolution problem (Sibarita, 2005) as one tries to *undo* the blurring from the imaging system. Since, within the fluctuations of the noise, several different  $O(i, j)$  can lead to the same image  $I_m$ , direct reconstruction is not uniquely possible. This is a well-known problem that can only be circumvented by constraining the set of allowed  $O(i, j)$ . Here, we do not formulate these constraints for the  $O(i, j)$  directly, but rather introduce a geometric model of the object shape, which indirectly determines the  $O(i, j)$ . In the following, we describe a shape model for endosomes. While this improves the clarity of presentation, it does not distract from the more general nature of the method. Applications to other objects or extensions to more complex shape models are readily possible.

The outline of an endosome  $k$  is represented by a piece-wise linear closed spline  $\vec{\theta}^k = [x_1^k, y_1^k, \dots, x_n^k, y_n^k]^T$ . This amounts to connecting  $n_k$  points along the endosome outline by straight lines. We limit the complexity of the outlines by introducing penalties  $E_b(\vec{\theta})$  and  $E_s(\vec{\theta})$  for local bending and stretching. These penalties quantify the mechanical deformation energy contained in an outline  $\vec{\theta}^k$  and counteract the tendency of over-fitting the outlines on insignificant image features.

The objects present in the imaging plane determine the object intensity function  $O(i, j)$ : Let  $S$  be the collection of all endosome outlines  $\vec{\theta}^k$  in an image. A constrained object intensity function  $O(i, j)$  is constructed by setting only the pixels  $(i, j)$  close to or enclosed by one of the outlines  $\vec{\theta}^k$  to non-zero values:

$$O(i, j) = \begin{cases} c^k & \text{if } (x_i, y_j) \text{ enclosed by } \vec{\theta}^k \\ (1-d)c^k & \text{if } d = D((x_i, y_j), S) < 1 \\ 0 & \text{else,} \end{cases} \quad (2)$$

where  $D$  is the distance to the closest outline  $\vec{\theta}^k$ , and  $c^k$  the fluorescence intensity inside endosome  $k$ . We compute the *hypothetical image*  $I$ , that would be expected if the outlines in  $S$  were indeed the true outlines of the endosomes, by using this object intensity function in Eq. (1).

Reconstructing the locations of the points  $\vec{\theta}^k$  on the endosome outlines is done by minimizing the *objective function*

$$Q(I_m, S) = E_{\text{image}}(I_m, I(S)) + \sum_k (E_b(\vec{\theta}^k) + E_s(\vec{\theta}^k)), \quad (3)$$

where the *image energy*  $E_{\text{image}}$  is computed by comparing the hypothetical image  $I$  to the actually observed image  $I_m$ :

$$E_{\text{image}} = \sum_i \sum_j (I_m(i, j) - I(i, j))^2. \quad (4)$$

This constitutes an adaptation of the active contour formulation by Kass et al. (1988).

Our outline reconstruction method proceeds in 5 algorithmic steps: (1) preprocessing the microscopy images, (2) detecting the objects in the image, (3) estimating the object intensities, (4) decomposing the image into smaller parts, and (5) reconstructing the precise outlines of all objects.

*Image preprocessing* reduces high-frequency noise and low-frequency background variations in the images. Noise reduction is important to allow robust segmentation based on image gradients. It is achieved by convolving the original image with a  $3 \times 3$  Gaussian kernel with standard deviation  $\sigma = 0.5$  pixel. Background variations have to be removed from the image since they comprise all non-object-specific signals that can not be accounted for by the present imaging and object models. We use a method related to the rolling ball algorithm (Sternberg, 1986). For each pixel in the raw image, the local background value is determined as the most frequently occurring intensity value in square region (typically  $15 \times 15$  pixels) centered at that pixel. The so-found background

image is then smoothed with a Gaussian kernel ( $9 \times 9$ ,  $\sigma = 2$  pixel) to reduce local variations. Subtracting the smoothed background image from the de-noised image yields a virtually background-free image.

In the next step, *objects are detected in the image*. This image segmentation procedure provides the initial locations for the outline reconstruction. For endosomes, an initial outline is given by a closed path of pixels that defines a segmentation of the image into fore- and background. In order to determine such a segmentation, we use the fact that the image of each endosome contains a local intensity maximum and is, therefore, enclosed by a ridge in the spatial intensity gradient. Intensity edges are highlighted by thresholding each pre-processed image followed by a convolution with a Laplacian of Gaussian kernel ( $5 \times 5$ ,  $\sigma = 0.2$  pixel). We then use the watershed transform (Vincent and Soille, 1991) to detect pixels that lie on ridges of the edge image and are, hence, close to the outline of an endosome. Connecting neighboring ridge pixels to closed paths yields the desired initial outlines to single-pixel resolution, without correcting for the blurring due to the microscope PSF.

The *object intensities*  $c^k$  of the endosomes are *estimated* in order to use them in Eq. (2) and as a biologically significant readout. For an endosome that is far larger than the width of the PSF, the object intensity is approximately equal to the central intensity  $\phi$  in the image of the endosome (top-right image in Fig. 1A). Smaller endosomes have a central intensity that is reduced by a factor  $\kappa$ . In order to estimate the reduction factor  $\kappa^k$  for a given endosome  $k$ , we analyze the radial intensity profile  $J(r)$  of the endosome (Fig. 1A). This profile is determined by averaging the intensities along concentric circles with different radii  $r$  around the endosome's intensity centroid. The half width at half maximum  $r_{0.5}$  of this profile serves as a dimension parameter (Fig. 1A). Since the dependence  $\kappa = f(r_{0.5})$  is not explicitly known, we empirically calibrate  $\kappa$  on synthetic images that are generated by convolving circular objects of different sizes and known object intensities  $c^i$  with the microscope PSF. For each synthetic image  $I^i$  we measure  $r_{0.5}^i$  and the central intensity  $\phi^i$ , and then compute the calibration function as  $\bar{\kappa}^i(r_{0.5}^i) = c^i / \phi^i$ . Based on this function, the object intensity  $c^k$  of an experimentally observed endosome can later be determined by interpolating  $\bar{\kappa}$  at the measured value  $r_{0.5}^k$  and multiplying with the central intensity  $\phi^k$ . For small, diffraction-limited objects,  $r_{0.5}$  converges to the half width at half maximum of the microscope PSF and does no longer vary with object size. Therefore, the analysis of sizes and shapes is restricted to larger objects. An endosome's with an  $r_{0.5}$  below an empirically determined threshold is treated as circular. Its center is fixed to the observed intensity centroid and the object intensity  $c$  is found by standard least squares regression based on Eqs. (4) and (1).

In order to speed up the computations and to allow outline reconstruction for different endosomes in parallel on different computer processors, we *decompose the image* into smaller, independent parts. This is based on the fact that the PSF  $P$  is of limited spatial extent such that the influence of endosomes on distant pixels in the image can be neglected. The width  $w$  where the PSF has decayed below 1% of its peak defines the radius of the region of influenced pixels around each endosome outline  $\vec{\Theta}^k$  (Fig. 1B). Endosomes with overlapping influence regions are grouped together and their influence regions are merged into a single region. This allows decomposing the image into independent rectangular sub-images  $I^l$  that comprise the merged influence regions (Fig. 1C). The image error term in Eq. (3) is now computed independently for each sub-image and we no longer consider points that are in no sub-image.

*Reconstructing the precise outlines of the endosomes* to sub-pixel resolution and correcting for the imaging characteristics of the microscope (PSF) is achieved by minimizing the objective function given in Eq. (3) with respect to the  $\vec{\Theta}^k$ . Since there is no mutual influence between endosomes in different sub-images  $I^l$ , their contributions to the objective function are minimized independently. Following the solution proposed by Kass et al. (1988), we use a gradient descent method with adaptive step size. This involves approximating the partial derivatives of the image energy  $E_{\text{image}}$  with respect to the  $x$  and  $y$  positions of all spline points  $(x_i^k, y_i^k)$ ,  $i = 1, \dots, n_k$ . In order to compute a finite difference approximation to the derivative in  $x$ -direction with respect to a point  $(x_i^k, y_i^k)$  on the outline  $\vec{\Theta}^k$  of endosome  $k$ , we displace the point by  $\Delta x$ . This yields a deformed hypothetical outline  $\vec{\Theta}_*^k$  and hence a new set of outlines  $S_*$ . The derivative of the image error  $E_{\text{image}}^l$  in sub-image  $I^l$  is then found as

$$\frac{\partial E_{\text{image}}^l}{\partial x_i^k} \approx \frac{E_{\text{image}}^l(I_m^l, I^l(S_*)) - E_{\text{image}}^l(I_m^l, I^l(S))}{\Delta x} \quad (5)$$

The derivatives with respect to other points and in the  $y$ -direction are found accordingly. The hypothetical sub-image  $I^l(S_*)$  needs to be computed once in each iteration of the minimization procedure. Minimization starts from the initial outlines as determined by the watershed transform (cf. step 2) and stops when the outlines do not significantly change any more between two subsequent iterations.

### 3. Results

The presented algorithm for reconstruction of intracellular structures enables quantification of processes in live cells that in-

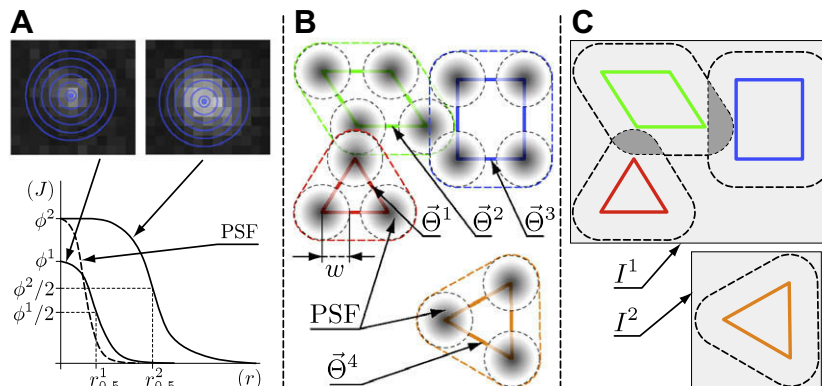


**Fig. 1.** (A) Radial intensity profile of a small (left image) and a large (right image) object found by averaging intensities along concentric circles. The intensity profile of the small object and the PSF (dashed line) have a similar shape. The wider shape of the intensity profile of the large object is reflected in an increased value of  $r_{0.5}$ . (B) The width of the PSF defines the extent of image regions (dashed lines) that are influenced by different objects  $\vec{\Theta}^k$  (solid lines). (C) Objects with overlapping influence regions (dark gray areas) are grouped together. Independent sub-images  $I^l$  (light gray rectangles) can be treated separately.

volve dynamic shape changes. After benchmarking the accuracy and precision of the algorithm as a function of the signal-to-noise ratio of the images, we exemplify the benefits of the present method in comparison to a classical pixel-based approach in three case studies that consider the shape and fusion dynamics of lipid-bounded endosomes. In all studies, we compare the results obtained from *refined* sub-pixel accurate outlines to the results obtained on the *unrefined* initial pixel-based segmentation.

### 3.1. Benchmarks

We assessed the performance and limitations of the outline refinement algorithm on two sets of synthetic data. The first set contained images of a circular object with a diameter of 500 nm, the second set contained images of a 200–400 nm wide and 900 nm long pear-shaped object. In both cases, synthetic objects were generated from the true outlines according to Eq. (2). The object intensity  $c$  was set to 200 and a background level of  $b = 20$  was added (Fig. 2D). Imaging was simulated by a convolution of the objects with the measured PSF of the experimental setup (full width at half maximum was 322 nm, see Section 5) and addition of Poisson-distributed noise (Fig. 2E and F). In order to add the proper physical noise level, we transformed the (gray-scale) image intensities  $I$  to expected photon counts  $\lambda$  using the linear function  $\lambda(i,j) = \eta I(i,j)$ . Noisy images were then obtained by sampling a new value for each pixel  $(i,j)$  from a Poisson distribution with parameter  $\lambda(i,j)$  and transforming back to gray-scale intensities. By varying  $\eta$ , we adjusted the signal-to-noise ratio  $\text{SNR} = (c - b)/\sigma_c$  in the range of 7–56, where  $\sigma_c$  is the noise level in the center of the objects. For each object and SNR,  $N=250$  sample images were generated and object outlines were fitted and compared to the true outline.

We quantified accuracy and precision of the fitted position (Fig. 2A), total intensity (Fig. 2B), and shape (Fig. 2C). The position error is defined as the difference between the true and detected  $x$ -position of the intensity centroid.<sup>1</sup> The total intensity error is given by the difference in total intensity (sum of all  $O(i,j)$  enclosed by the outline) between the reconstructed object and the true synthetic object, divided by the total intensity of the true synthetic object. The shape error is defined as the sum of non-overlapping areas of the true and fitted outlines, normalized by the area enclosed by the true outline. Lines depicting the  $\pm$  standard error interval are shown in the bias plots in order to enable visual assessment of the significance. The standard error is given by the estimated standard deviation divided by  $\sqrt{N}$ .

For both shapes, precision and accuracy of the measured position are in the range of a few nanometers (Fig. 2A). The errors in the  $y$ -direction are comparable for the pear-shaped object and identical for circular shapes (data not shown). The position bias for the circular shape (dashed lines) is always within the  $\pm 1$  standard error interval, and hence not significant. As expected, a small systematic position bias can be observed for the pear-like shape (solid lines). Since the shape is not symmetric, the systematic underestimation of high curvature causes a small shift in the position estimate towards the less complex side. For both shapes the standard deviation of the relative total intensity error drops below 5% for SNRs larger than 10 (Fig. 2B). The bias, however, is larger than the standard error, almost always negative, and converges to about  $-1\%$ . This is due to the stretching penalty  $E_s$  in Eq. (3), which favors shrinking of outlines and thereby decreases the integrated object intensity function. The means and standard devia-

tions of the shape errors of both shapes converge to values of less than 10% and 3%, respectively (Fig. 2C). The bending and stretching penalties  $E_b$  and  $E_s$  prevent the mean shape error from converging to zero, and the systematic underestimation of high curvature causes an additional bias for the more complex pear-shaped object. Nevertheless, we observe that the reconstructed outlines visually reproduce well the essential characteristics of the true outline, even at SNRs below 15 and therefore error levels of more than 10% (Fig. 2G).

### 3.2. Endosome dynamics in live cells and characterization of fusion events

We analyzed live human embryonic retinoblast (HER) 911 cells stably expressing the small GTPase Rab5 tagged with enhanced green fluorescent protein (911-EGFP-Rab5) (Roberts et al., 1999). In order to capture the dynamics of endosome fusion events, 2.2  $\mu\text{m}$  thick  $z$ -stacks, comprising four images each, were recorded in the cell periphery at high frequency (25 stacks/s) on a spinning disc confocal microscope. After acquisition, the stacks were reduced to single images by maximum projection (Rink et al., 2005). Selected frames of a movie are shown in Fig. 3A. The outlines of the endosomes were reconstructed in each frame of the movie and individual detections were linked over time, yielding endosome trajectories (Sbalzarini and Koumoutsakos, 2005).

We quantify the dynamics of endosome shapes and fusion events by the time evolution of endosome area, total fluorescence intensity of each endosome, its eccentricity, and its concavity. These shape features were directly computed from the outlines as reconstructed by the present algorithm (see Section 5). Because the algorithm implicitly corrects for the microscope optics, computation of shape features is more robust and accurate than in standard pixel-based methods. In the latter, shape features can of course also be defined, but they are at best correlated with the features of the real objects.

The dynamics of the endosome shape features computed from refined outlines are shown in Fig. 3. Pronounced changes in endosome shape features were associated with topological and morphological changes of the endosomes. At 0.92 s, a large endosome (Fig. 3A, red outline) rapidly approached an immobile one (blue outline) until the two structures could no longer be resolved. At 1.08 s, the algorithm detected only a single outline. In the following, the endosome remained stationary before it coherently displaced along a linear track as a single entity (4.08 s). We conclude that the merged object represented a fused endosome with different dynamic behavior. A transient peak in concavity and eccentricity during about 0.12 s marked the fusion event (Fig. 3B, blue lines). As expected, the area increased upon fusion, and the total fluorescence intensity of the fused endosome matched the sum of the two pre-fusion intensities (Fig. 3B, red line and blue line). In contrast, the features of a stationary endosome remained constant (green lines).

We conclude that the changes in area and intensity, together with the sharp peaks in concavity and eccentricity, can be used as hallmarks of fusion events. We note that fusions are very fast events and that, therefore, high temporal resolution is required to detect the accompanying transient changes in morphological features. The present shape reconstruction algorithm enables automatic, unbiased, and reproducible estimation of shape features at high resolution. It therefore provides a prerequisite for detecting and analyzing fusion events (see also Fig. 5C).

### 3.3. Time course of endosomal virus sorting

We demonstrate the benefits of refined endosome outlines in analyzing virus trafficking through the endosomal network. The

<sup>1</sup> We prefer this definition over the classical Euclidean distance in  $(x,y)$  because it enables correlating shape asymmetries with the position errors in the different directions.

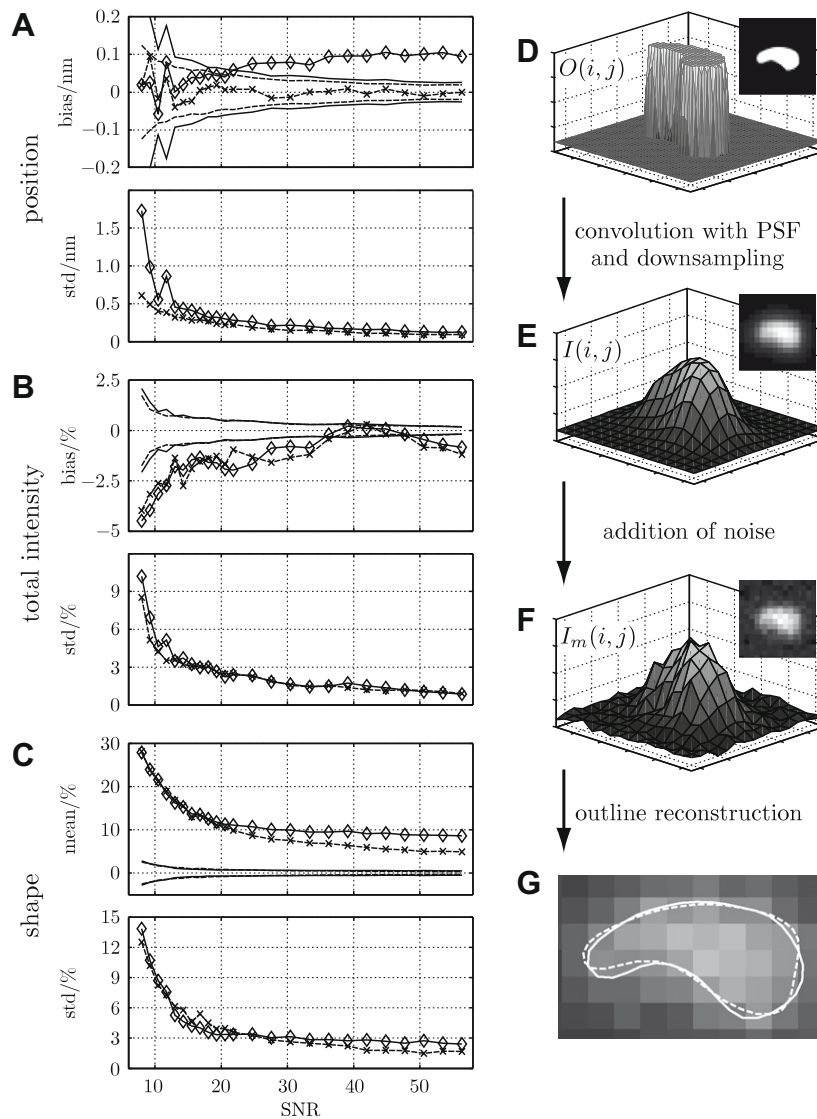


**Fig. 2.** (A–C) Benchmark results on synthetic images. Accuracy (bias) and precision (std) of the reconstructed position (A), total intensity (B), and shape (C) of a pear-shaped (solid lines with diamonds) and a circular (dashed lines with crosses) object are shown. Lines without markers delimit the  $\pm 1$  standard error interval ( $\text{std}/\sqrt{N}$ ,  $N = 250$ ). (D–F) Generation of synthetic test images. The object intensity function  $O(i, j)$  (Eq. (2))(D) is blurred by convolution with the PSF (E) and noise is added (F). (G) True outline (solid line) and the outline estimated at an SNR of 12.5 (dashed line). The shape error in this example was 14%.

trafficking of virus particles can be monitored by quantifying the colocalization of endosomal and viral markers (Bolte and Cordeliers, 2006). Here we used human Adenovirus type 2 (Ad2) and human Ad2-ts1 (temperature-sensitive 1, TS1), a mutant of Ad2 that visits early endosomes like wild-type Ad2, but fails to escape to the cytosol and is instead delivered to late endosomes and lysosomes (Gastaldelli et al., 2008). Fluorescently labeled virus particles were bound to HER 911-EGFP-Rab5 cells and internalized at 37 °C. Image stacks of Rab5-positive endosomes and virus particles were recorded from single cells during the first 45 minutes of the infection (see Section 5). Supplementary Fig. 1 shows the two color channels (green: EGFP-Rab5, red: TS1-atto647) separately and overlaid for a cell imaged 10 min post-infection. The overlay shows that some viruses seem to colocalize with Rab5. The degree of colocalization and its significance, however, can not be estimated by eye.

We therefore reconstructed the endosome outlines from maximum-projected image stacks and determined the virus positions by intensity centroid estimation (see Section 5). We defined colocalization as the fraction of viruses that were enclosed by an endosome outline (see Fig. 4A and B and insets therein). In order to

compare the present method to previous approaches, we consider both refined and unrefined outlines. While the unrefined outlines are certainly correlated with the true outlines, they are likely to be biased and more sensitive to variations in individual pixel intensities. Fig. 4A and B support this argument: Considering the blurring introduced by the microscope PSF, the unrefined outlines are clearly too wide. In Fig. 4C and D we show the histogram of distances of viruses to the nearest endosome outline. Compared to the refined outlines (D), the distribution for the unrefined outlines (C) has a broader peak and is shifted toward smaller distances.

In order to test how these differences affect the final results, we determined the colocalization scores of Ad2 (Greber et al., 1993) and its temperature-sensitive mutant TS1 (Greber et al., 1996) with EGFP-Rab5 using either refined or unrefined outlines. It is known that Ad2 escapes from an endosome soon after internalization (Greber et al., 1993). We thus expect little colocalization of Ad2 with Rab5. In contrast, the signaling-incompetent mutant TS1 is known to reside in early endosomes and lysosomes during the first hour of entry into cells (Greber et al., 1996; Gastaldelli et al., 2008), probably yielding a transient, but long-lasting, in-

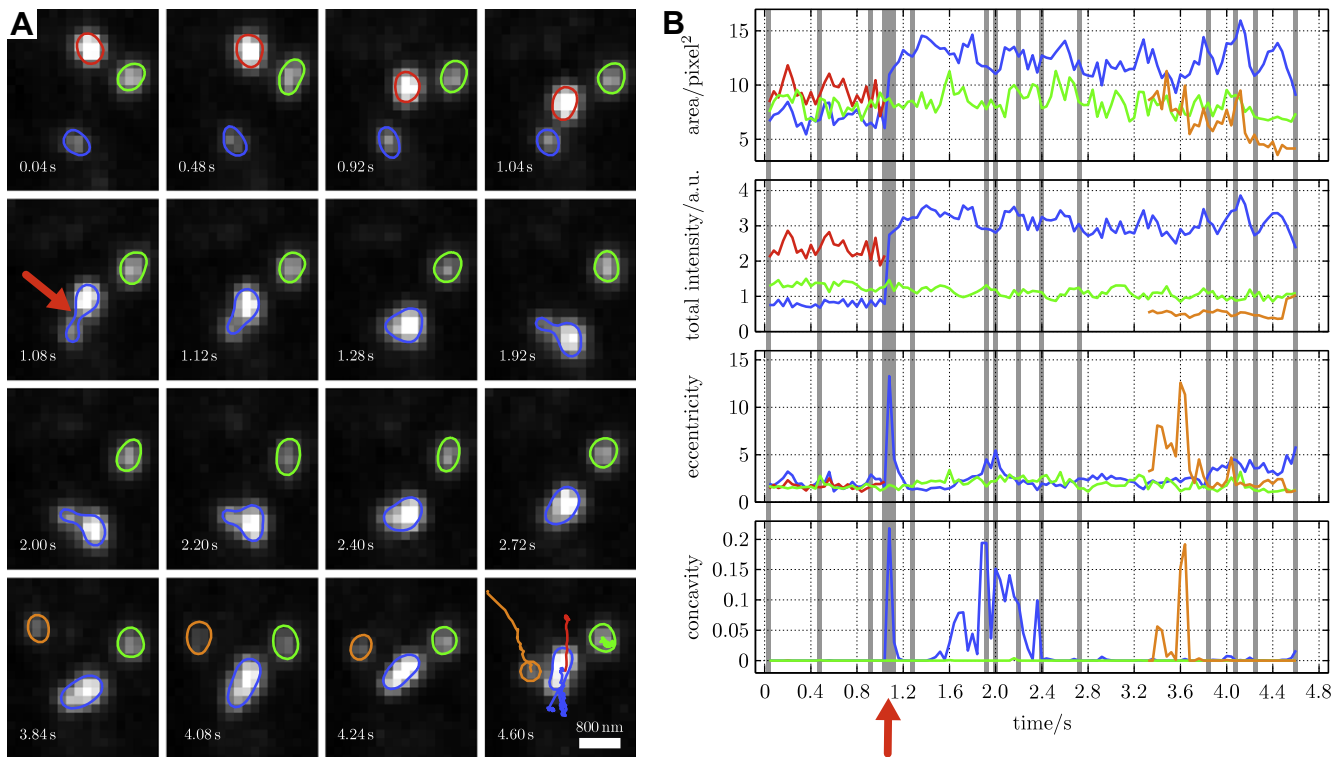


**Fig. 3.** Dynamic shape changes of Rab5-positive endosomes. (A) A region near the periphery of an HER 911 cell, imaged at 25 Hz, expressing GFP-Rab5. Selected frames with overlaid outlines as reconstructed by the present algorithm are shown. Trajectories of the endosomes are shown in the last frame. (B) Area, total intensity, eccentricity, and concavity are plotted for the indicated objects in (A) during a period of 4.6 s. Gray vertical lines mark time points of the frame images in (A) and color correspondence identifies endosomes).

crease in colocalization with Rab5. The colocalization scores were determined for 201 (Ad2) and 184 (TS1) cells, each one imaged at a single time point between 0 and 45 min post-infection.

In order to estimate the degree of unspecific colocalization, we performed controls with randomized virus positions (see Section 5). Individual colocalization scores were weighted proportionally to the number of viruses detected and their means and standard deviations over time were estimated using a Nadaraya–Watson kernel estimator with bandwidth  $h = 3$  min (Simonoff, 1998). The time courses of Ad2 and TS1 colocalization with Rab5-positive endosomes are shown in Fig. 4E and F. The level of unspecific colocalization that would be expected under random placement of viruses was approximately 1–5% for refined outlines and 2–10% for unrefined outlines.

The mean colocalization score for Ad2 remained constant on a comparably low (but above background) level of less than 10% when using refined outlines (Fig. 4F, lower line). The score for TS1 (upper line) showed an increase from 12 to 20% between 10 and 20 min post-infection and then remained high throughout the observation period. For both viruses, the  $\pm 1$  standard deviation intervals (light gray areas) are narrow and do mostly not overlap (dark gray areas). In summary, Ad2 and TS1 show colocalization signatures that are significantly distinct in magnitude and dynamics and that are in good agreement with prior observations (Greber et al., 1993, 1996; Gastaldelli et al., 2008).

This picture is much less clear when using unrefined outlines. While the increase around 15 min post-infection is still apparent for TS1 (upper line), the score for Ad2 (lower line) increases faster from 0 to 45 min post-infection than when using refined outlines (Fig. 4E). Compared to the results based on refined outlines, we observe larger means and standard deviations (gray shaded areas) for both viruses. The  $\pm 1$  standard deviation intervals significantly

overlap during the entire observation period (dark gray areas). This makes it difficult to robustly distinguish between the two viruses. In summary, the qualitative and quantitative trends seen in Fig. 4E are not in agreement with prior observations (Greber et al., 1993, 1996; Gastaldelli et al., 2008).

#### 3.4. Endosome shape features in virus-infected cells

We demonstrate the benefits of the present algorithm in large-scale studies of shape and dynamics. In Section 3.2, we have shown that our algorithm enables robust and accurate quantification of dynamic changes such as fusion events. This was based on the estimation of a set of descriptive shape features. Since the present method is completely automatic, it enables processing of large amounts of data in an unbiased and reproducible way. This leads to increased statistical significance of the final results. We demonstrate this by applying the present algorithm to estimate the shape features of all endosome outlines in all 201 and 184 cells infected with Ad2 and TS1, respectively. As a control we recorded and analyzed images of 31 non-infected cells. The measured distributions for area and total intensity are shown in Fig. 5A and B for the control (solid black lines, “control”) and TS1-infected cells (dashed blue lines, “all TS1”). The results for the other shape features and for Ad2 were of equal quality (figures not shown).

Using these distributions, we addressed the question whether viruses preferentially occupy endosomes with specific shape features. We focused on the subset of Rab5 endosomes that enclosed at least one TS1 particle. Comparison of the shape feature distributions of this set (“TS1 (+)”) with the distributions of all Rab5 endosomes (“all TS1”) showed that viruses were more frequently found in large endosomes with high fluorescence intensity (Fig. 5A and B, dash-dotted green lines). This preference was significantly stronger

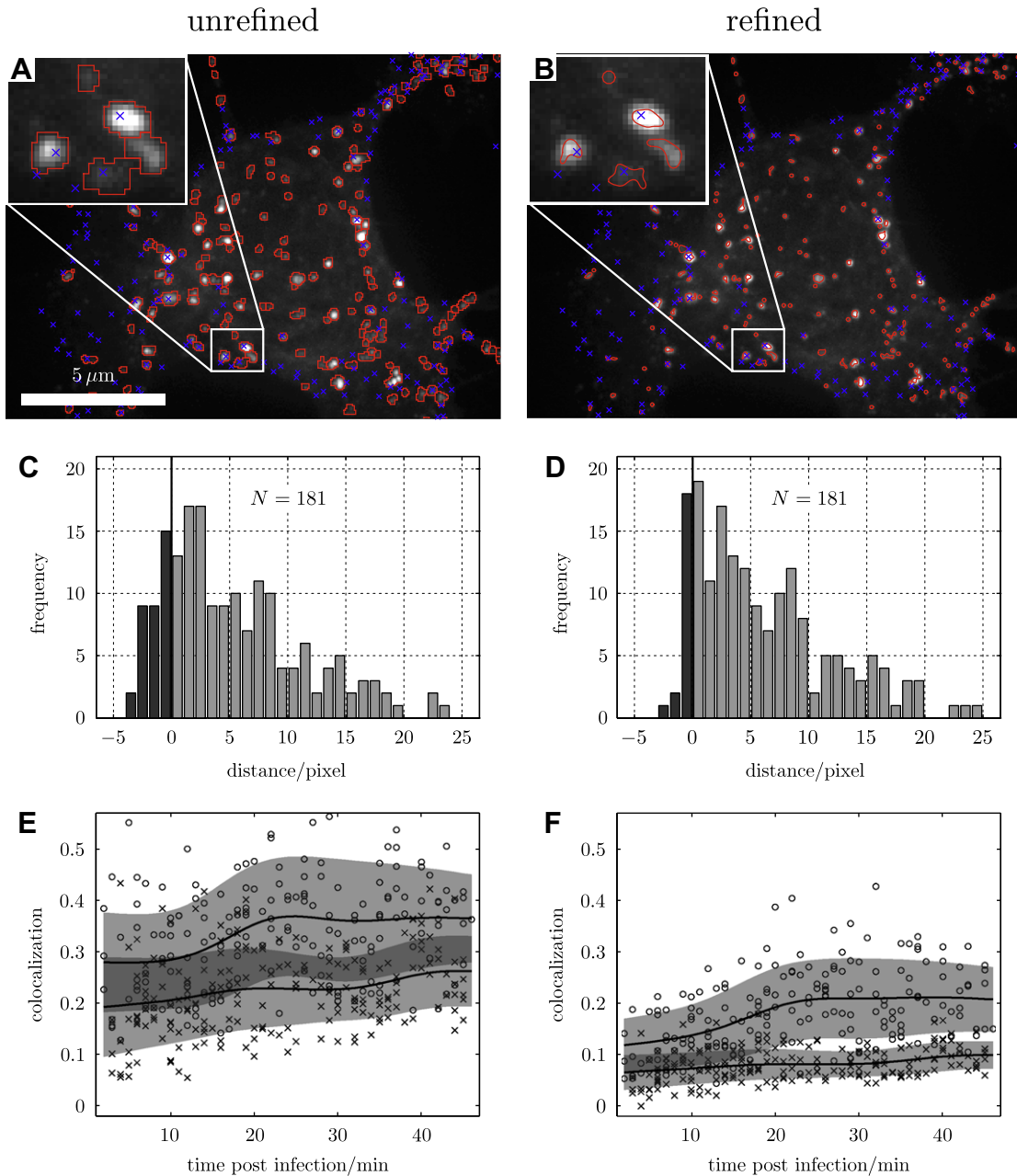


**Fig. 4.** Dynamics of endosomal virus sorting studied using unrefined (A, C, E) outlines and outlines refined by the presented algorithm (B, D, F). (A,B) HER-911 cell expressing EGFP-Rab5 imaged 10 min post-infection with overlaid endosome outlines (red lines) and positions of TS1 virus particles (blue crosses). (C,D) Histograms of distances of viruses to the nearest point on an endosome outline for the example cell shown in (A) and (B). Negative distances (dark gray bars) correspond to viruses inside endosomes. (E,F) Comparison of the time-course of mean (black lines) and  $\pm 1\sigma$  interval (light gray shaded areas) of the colocalization scores for Ad2 (lower line) and TS1 (upper line) based on unrefined (E) and refined (F) outlines. The scores for individual cells are shown as crosses (Ad2,  $N = 201$ ) and circles (TS1,  $N = 184$ ). The dark gray areas mark the overlap between the two  $\pm 1\sigma$  intervals. (For interpretation of the references to color in this figure legend, the reader is referred to the web version of this paper.)

than what would be expected when randomly placing the viruses in the cell (“randomized TS1 (+)”, dotted red lines, see Section 5), ruling out a linear dependence of the frequency of occupation on endosome area. Virus-containing endosomes only showed slightly increased concavity (Fig. 5C) compared to the population of all endosomes in the cell. Using the randomized virus positions (“randomized TS1 (+)”), a clear trend toward higher concavities was observed, which is consistent with the fact that the outline shapes can be better resolved on larger scales.

We compare the shape feature distributions obtained using the refined outlines to those from unrefined outlines. For area and total intensity (data for unrefined outlines not shown), the distributions

showed the same trend when comparing TS1-containing endosomes to the population of all endosomes, although the trend was less significant. For concavity, the results look very different (Fig. 5C). In unrefined outlines (right peak), high concavity ( $>0.3$ ) was virtually non-existent and there was a pronounced peak around 0.1, which can be attributed to the step-like non-smooth shape of the outlines. This significantly reduces the information content of the observations. Consider for example the fusion case shown in Figs. 3 and 5C (insets). When using refined outlines (left peak), the concavity increased from 0 to 0.2 during the fusion of the endosomes. On unrefined outlines, an uninformative change from 0.09 to 0.12 was measured (Fig. 5C, horizontal distance ar-

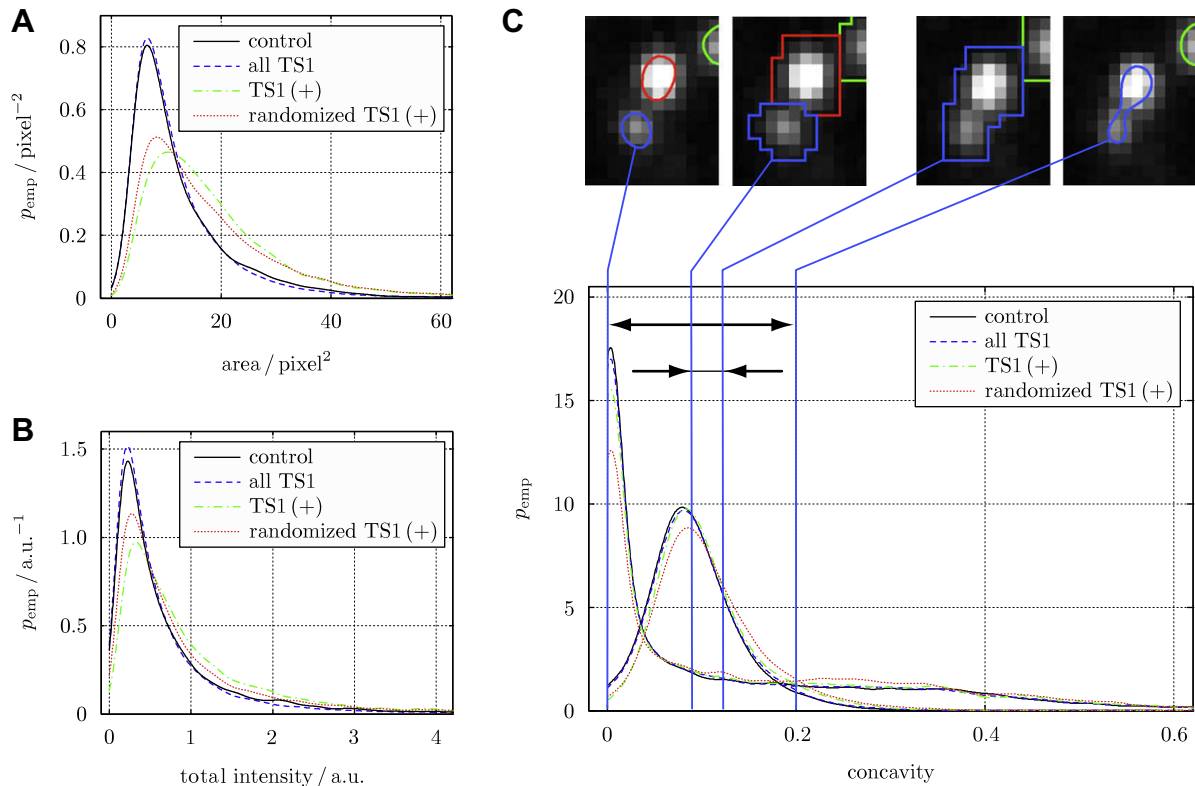


**Fig. 5.** Shape features of Rab5-positive endosomes in HER-911 cells. Empirical distributions of endosome area (A), total intensity (B), and concavity (C) are shown for refined outlines. Each panel shows the distributions for: all endosomes in non-infected control cells (solid black lines,  $N = 4581$ ), all endosomes in cells infected with TS1 (dashed blue lines,  $N = 31351$ ), endosomes containing at least one TS1 particle (dash-dotted green lines,  $N = 4119$ ), and endosomes containing at least one TS1 particle with randomized position (dotted red lines, average  $N = 3458$ ). All distributions were estimated using a Gaussian kernel density estimator with bandwidth  $h = 2 \text{ pixel}^2$  (A),  $h = 0.1 \text{ a.u.}$  (B),  $h = 0.0125$  (C). (C) compares the distributions from unrefined (right peak) and refined (left peak) outlines. The inset images in (C) compare the shapes immediately before and after the fusion event shown in Fig. 3A. Using refined outlines, the change in concavity is more pronounced (horizontal distance arrows). (For interpretation of the references to color in this figure legend, the reader is referred to the web version of this paper.)

rows). Detection of shape change events, such as fusion, may thus depend on the use of properly refined outlines.

We further formalize the benefits of using the present shape refinement algorithm by applying statistical tests to the shape feature distributions. We used a two-sided Kolmogorov–Smirnov test on the null hypothesis that the shape feature distributions are identical. We tested all possible combinations of the three cases of TS1-infected cells, Ad2-infected cells, and control cells without virus, considering *all* endosomes in each cell, and not only those that actually contained virus(es). The results are summarized in Fig. 6A and B. The  $p$ -values are color-coded according to the significance level and the signs indicate the directions of the shifts of the means. The present algorithm enables unbiased processing of large amounts of data. This led to rejection of the null hypothesis in some cases, despite the small visual differences between the distributions (Fig. 5A and B, “all TS1” vs. “control”). We assess the self-consistency of the results obtained using unrefined and refined outlines. The test results for refined outlines (Fig. 6A) show a consistent picture: TS1-infection significantly changes area, total intensity, and eccentricity (red and orange colors in first row), but Ad2-infection does not (green and yellow colors in second row). The third row, comparing TS1 against Ad2, confirms this result. When using unrefined outlines, the test outcomes are self-inconsistent (Fig. 6B) and do not support any conclusion. Furthermore, area and total intensity are correlated quantities and the color patterns of these two columns should be similar. While this is the case when using refined outlines, the patterns for unrefined outlines look opposite.

In summary, the results of this test case show the benefits of automatic reconstruction of large amounts of refined endosome outlines. This allowed accurate and self-consistent quantification of shape features. The resulting distributions were free of obvious quantification artifacts and revealed differences between populations of endosomes. The large amounts of unbiased data further enabled statistical detection of subtle changes in feature distributions in a self-consistent way.

#### 4. Conclusions and discussion

We devised a novel model-based method to reconstruct outlines of subcellular structures from fluorescence microscopy images to a sub-pixel representation. The method is based on image segmentation and iterative regularized optimization of a geometric model of the outlines. During optimization, a physical model of image formation is used to generate hypothetical images from estimated outlines. At each iteration, the quality of the estimate is evaluated by comparison with the experimentally observed image.

Without distracting from the more general applicability of the method, we presented a specific object model for endosomes and validated the method on synthetic data resembling images of endosomes at different SNRs. Our imaging protocol was a compromise between imaging speed and signal intensity, which resulted in SNRs in the range of 10–30. In this range, errors in position and fluorescence intensity estimates were below 1 nm and 5%, respectively. Although the method systematically underestimated

A	refined				p-value
	area	tot. int.	ecc.	conc.	
TS1 / Ctrl	$8.6 \cdot 10^{-4}$ (-)	$2.0 \cdot 10^{-6}$ (-)	$2.5 \cdot 10^{-4}$ (+)	$5.1 \cdot 10^{-1}$ (+)	
Ad2 / Ctrl	$8.4 \cdot 10^{-1}$ (+)	$1.4 \cdot 10^{-2}$ (-)	$3.6 \cdot 10^{-2}$ (+)	$8.4 \cdot 10^{-1}$ (+)	
TS1 / Ad2	$1.9 \cdot 10^{-10}$ (-)	$9.4 \cdot 10^{-9}$ (-)	$3.0 \cdot 10^{-14}$ (+)	$4.6 \cdot 10^{-1}$ (+)	

B	unrefined				p-value
	area	tot. int.	ecc.	conc.	
TS1 / Ctrl	$2.4 \cdot 10^{-2}$ (-)	$6.7 \cdot 10^{-6}$ (-)	$5.4 \cdot 10^{-5}$ (+)	$1.5 \cdot 10^{-1}$ (+)	
Ad2 / Ctrl	$3.9 \cdot 10^{-2}$ (+)	$1.2 \cdot 10^{-3}$ (-)	$1.2 \cdot 10^{-1}$ (+)	$7.4 \cdot 10^{-1}$ (+)	
TS1 / Ad2	$4.2 \cdot 10^{-6}$ (-)	$2.5 \cdot 10^{-2}$ (-)	$9.0 \cdot 10^{-10}$ (+)	$1.1 \cdot 10^{-2}$ (+)	

**Fig. 6.** Self-consistence of statistical tests on the shape feature distributions. The *p*-values of two-sided Kolmogorov–Smirnov tests of the null hypothesis of identical distributions are shown (color codes significance level). First row: all endosomes in TS1-infected cells (“all TS1” in Fig. 5,  $N = 31351$ ) versus control cells (“control” in Fig. 5,  $N = 4581$  endosomes); second row: all endosomes in Ad2-infected cells ( $N = 34323$ ) versus control ( $N = 4581$  endosomes); third row: TS1-infected cells (“all TS1” in Fig. 5) versus Ad2-infected cells. Signs mark the direction of the trend with a (+) denoting that the first condition had a larger mean feature value than the second one, and a (-) the opposite. The self-consistence of the test results based on refined outlines (A) is compared to that from unrefined outlines (B).

the curvature of outlines, the essential characteristics of the shapes were captured, even at low SNRs. When applied to experimental data, the main limitation of the method is that outline topology cannot change during optimization. The topology of the outlines is defined by the initial segmentation, which can be ambiguous if objects are close to each other. An implicit representation of the outlines as level sets could potentially circumvent this limitation (Machacek and Danuser, 2006; Sethian, 2001). In addition, our object model uses spatially constant fluorescence intensities inside objects. While more complex object intensity models could easily be constructed and used, they would be more prone to over-fitting and regression instability. In addition, we identified only few situations where they would be beneficial. If sufficient experimental data about the actual fluorescence intensity distribution inside a single object were available, this knowledge could, however, be accounted for in more complex object intensity models.

We then applied the presented algorithm to study the dynamics of Rab5-positive endosome fusion events at 25 Hz temporal resolution. The object representation as smooth closed splines allowed measuring the eccentricity and concavity of endosome outlines. These features showed a characteristic pattern during endosome fusion and could be used to automatically detect fusion events. Moreover, the total intensity and area of endosomes were estimated with high accuracy and precision. We found that Rab5 fluorescence intensity exhibited little fluctuations, suggesting that the total amount of Rab5 in the endosomal membranes remained constant over the fusion event. Rab5 could thus have a function both before and after fusion of the endosomes.

When applied to virus trafficking, the proposed method yielded precise and realistic maps of the positions of virus particles with respect to endosome membranes. We defined a colocalization score as the fraction of viruses that were enclosed by endosome outlines. Based on the refined outlines, the time-courses of colocalization of Adenovirus serotype 2 (Ad2) and its temperature-sensitive mutant TS1 with Rab5-positive endosomes were in good agreement with earlier observations (Greber et al., 1996; Gastaldelli et al., 2008). Unrefined outlines found by pixel-based image segmentation, on the other hand, led to an ambiguous and inconsistent picture. Analysis of the shape feature distributions of Rab5-positive endosomes occupied by TS1 revealed that, among all endosomes in a TS1-infected cell, this virus is preferentially found in a sub-population of larger endosomes with elevated fluorescence intensity. Since TS1, but not Ad2, depends on active Rab5 (Gastaldelli et al., 2008), it is possible that TS1 activates Rab5 and that this contributes to the enlargement of TS1-containing early endosomes (Bucci et al., 1992). Comparing the refined outlines of all endosomes in TS1-, Ad2-, and non-infected cells, we could detect a global, but subtle effect of TS1 infection. This effect was sta-

tistically significant thanks to the large amount of unbiased data delivered by the presented fully automated method.

Taken together, our method for highly accurate object outline reconstruction enabled conclusive observations that were previously impossible. This is because pixel-based segmentation procedures detect *local structures* in the image data, whereas the present outline refinement algorithm *explains* the image data based on the outline estimates. When the sub-cellular structures are small compared to the resolving power of the microscope, this can greatly reduce relative errors in the outline estimates. We demonstrated that this is of great importance for the detection of fusion events and for colocalization analysis of virus trafficking through the endosomal network. The proposed outline refinement increased the discriminative power and self-consistence of comparative studies using statistical tests. With minor adaptations of the shape model and initialization procedure, the presented algorithm can be applied to analyze the shapes of other small and compact organelles such as late endosomes, lysosomes, peroxisomes, caveosomes, mitochondria, or nuclei. We thus anticipate that the combination of flexible shape models and implicit deconvolution will be generally beneficial to many subcellular imaging studies.

## 5. Materials and methods

### 5.1. Plasmids

The construct expressing GFP-Rab5 was obtained from Philipp Stahl (Washington University School of Medicine, St. Louis, MO).

### 5.2. Cells, viruses, and reagents

Human embryonic retinoblast 911 cells obtained from Dr. A. van der Eb (University of Leiden, The Netherlands) were grown in Dulbeccos Modified Eagle Medium (Sigma) plus 7% fetal bovine serum (Gibco). To obtain cells stably expressing EGFP-tagged Rab proteins, they were electroporated (T820, BTX), grown under G418 selection (Calbiochem), and sorted with a FACSAria cell-sorting system (Becton–Dickinson). For live cell microscopy, cells were grown on glass cover slips (Assistant Glaeser) of  $0.17 \pm 0.01$  mm thickness to match the correction of the objective. Ad2 and the temperature sensitive mutant TS1 were grown, isolated, and labeled with the fluorescent dye atto647 (Atto-tec) as described (Nakano and Greber, 2000).

### 5.3. Spinning disc live cell microscopy

Images were recorded with an NA 1.35 UplanApo100X objective on an Olympus IX81 inverted microscope (Olympus) equipped with a Yokogawa scanning head QLC100 (VisiTech International),

containing a triple bandpass excitation filter (488 nm/565 nm/647 nm, Chroma), and a NV 40/1CL piezo stepper for objective positioning (Piezosystem Jena). Images were recorded onto a Cascade 512 electron multiplying charge coupled device camera (Photometrics) with  $16 \times 16 \mu\text{m}^2$  pixel size. Image acquisition was controlled using MetaMorph software (Molecular Devices). Original unprocessed intensities were stored as uncompressed 16 bit bitmaps. Time lapse experiments of a total of 500 time points were recorded with 4 layers per z-stack. For virus infection experiments, an additional  $1.6\times$  lens of the microscope was used and 8 images per z-stack were acquired. Due to the short illumination times, bleaching was not observable in any of the experiments and no bleaching correction schemes were applied.

#### 5.4. Point spread function measurement

Image stacks of TetraSpeck multicolor fluorescent beads (Molecular Probes) were recorded and a maximum projection performed. Assuming radial symmetry, the PSF of the microscope was measured by averaging intensities along concentric circles centered at the intensity centroid in the maximum-projected image (Sibarita, 2005) (see Fig. 1A for illustration).

#### 5.5. Endosome shape features

Area was computed as the area enclosed by an outline  $\vec{\Theta}^k$ . Total intensity was area multiplied by the object intensity  $c^k$ . Eccentricity was computed from the radius of gyration tensor  $G$  of the surface enclosed by  $\vec{\Theta}^k$ . It was defined as the ratio between the largest and the smallest Eigenvalue of  $G$ . Concavity was computed from the area  $A_{ch}$  of the convex hull of an outline. It was defined as the ratio  $(A_{ch} - A)/A_{ch}$ , where  $A$  was the area enclosed by the outline. Features of unrefined outlines were computed in the same way.

#### 5.6. Virus position estimation

Virus positions were detected from maximum-projected image stacks by intensity centroid estimation as described (Sbalzarini and Koumoutsakos, 2005). To correct for potential effects of chromatic aberration on colocalization results, we estimated the lateral shift of the red (647 nm, viruses) relative to the green (488 nm, endosomes) channel in the full field of view. 200 nm multi-color TetraSpeck fluorescent beads (Molecular Probes) were bound to a cover slide and imaged in the red and green channels sequentially. The positions of the beads were determined by intensity centroid estimation in both channels. We observed a maximum lateral shift between the red and green channels in the order of 50 nm. This shift linearly depended on the  $x$  and  $y$  position of the bead in the field of view. We estimated this dependence by linear least squares regression from the bead data and used this to correct all virus position measurements as described (Kozubek and Matula, 2000).

#### 5.7. Software

All software was implemented in MATLAB (The MathWorks, Inc.) or C. The source code is available from the authors upon request. An implementation of the presented algorithm in the open-source image processing software ImageJ is currently under development and will be made freely available.

#### 5.8. Randomization control

Randomized virus positions were obtained by uniformly distributing all detected virus particles inside each cell. Cell outlines were found from the image of the endosomes by background re-

moval, strong low-pass filtering, and thresholding. All statistics of the randomization control were averaged over 10 independent realizations of the randomization process.

#### Acknowledgments

This work was supported by grants from the Swiss National Science Foundation (to U.F.G.) and the Novartis Foundation (to C.J.B. and U.F.G.). J.A.H. was financed by the ETH Research Commission under grant TH-1007-1. We thank the anonymous reviewers for their suggestions, which greatly helped improving the manuscript.

#### Appendix A. Supplementary data

Supplementary data associated with this article can be found, in the online version, at doi:10.1016/j.jsb.2009.03.017.

#### References

- Bolte, S., Cordelières, F.P., 2006. A guided tour into subcellular colocalization analysis in light microscopy. *J. Microsc.* 224, 213–232.
- Bucci, C., Parton, R.G., Mather, I.H., Stunnenberg, H., Simons, K., Hoflack, B., Zerial, M., 1992. The small GTPase Rab5 functions as a regulatory factor in the early endocytic pathway. *Cell* 70 (5), 715–728.
- Cheezum, M.K., Walker, W.F., Guilford, W.H., 2001. Quantitative comparison of algorithms for tracking single fluorescent particles. *Biophys. J.* 81, 2378–2388.
- Danuser, G., Stricker, M., 1998. Parametric model fitting: from inlier characterization to outlier detection. *IEEE Pattern Anal.* 20, 263–280.
- Gastaldelli, M., Imelli, N., Boucke, K., Amstutz, B., Meier, O., Greber, U.F., 2008. Infectious adenovirus type 2 transport through early but not late endosomes. *Traffic* 9, 2265–2278.
- Giepmans, B.N.G., Adams, S.R., Ellisman, M.H., Tsien, R.Y., 2006. Review—the fluorescent toolbox for assessing protein location and function. *Science* 312, 217–224.
- Greber, U.F., Webster, P., Weber, J., Helenius, A., 1996. The role of the adenovirus protease in virus entry into cells. *EMBO J.* 15, 1766–1777.
- Greber, U.F., Willetts, M., Webster, P., Helenius, A., 1993. Stepwise dismantling of adenovirus-2 during entry into cells. *Cell* 75, 477–486.
- Hayashi, M., Raimondi, A., O’Toole, E., Paradise, S., Collesi, C., Cremona, O., Ferguson, S.M., De Camilli, P., 2008. Cell- and stimulus-dependent heterogeneity of synaptic vesicle endocytic recycling mechanisms revealed by studies of dynamin 1-null neurons. *Proc. Natl. Acad. Sci. USA* 105, 2175–2180.
- Hell, S.W., 2007. Far-field optical nanoscopy. *Science* 316, 1153–1158.
- Kass, M., Witkin, A., Terzopoulos, D., 1988. Snakes: Active contour models. *Int. J. Computer Vision*, 321–331.
- Kozubek, M., Matula, P., 2000. An efficient algorithm for measurement and correction of chromatic aberrations in fluorescence microscopy. *J. Microsc.* 200, 206–217.
- Li, C.H., Bai, L., Li, D.D., Xia, S., Xu, T., 2004. Dynamic tracking and mobility analysis of single GLUT4 storage vesicle in live 3T3-L1 cells. *Cell Res.* 14, 480–486.
- Machacek, M., Danuser, G., 2006. Morphodynamic profiling of protrusion phenotypes. *Biophys. J.* 90, 1439–1452.
- Mellman, I., Warren, G., 2000. The road taken: past and future foundations of membrane traffic. *Cell* 100, 99–112.
- Nakano, M.Y., Greber, U.F., 2000. Quantitative microscopy of fluorescent adenovirus entry. *J. Struct. Biol.* 129 (1), 57–68.
- Neumann, B., Held, M., Liebel, U., Erfle, H., Rogers, P., Pepperkok, R., Ellenberg, J., 2006. High-throughput RNAi screening by time-lapse imaging of live human cells. *Nat. Methods* 3 (5), 385–390.
- Nickell, S., Kofler, C., Leis, A.P., Baumeister, W., 2006. A visual approach to proteomics. *Nat. Rev. Mol. Cell Bio.* 7, 225–230.
- Rink, J., Ghigo, E., Kalaidzidis, Y., Zerial, M., 2005. Rab conversion as a mechanism of progression from early to late endosomes. *Cell* 122, 735–749.
- Roberts, R.L., Barbieri, M.A., Pryse, K.M., Chua, M., Stahl, P.D., 1999. Endosome fusion in living cells overexpressing GFP-rab5. *J. Cell Sci.* 112, 3667–3675.
- Sbalzarini, I.F., Koumoutsakos, P., 2005. Feature point tracking and trajectory analysis for video imaging in cell biology. *J. Struct. Biol.* 151 (2), 182–195.
- Sbalzarini, I.F., Mezzacasa, A., Helenius, A., Koumoutsakos, P., 2005. Effects of organelle shape on fluorescence recovery after photobleaching. *Biophys. J.* 89 (3), 1482–1492.
- Sethian, J.A., 2001. Evolution, implementation, and application of level set and fast marching methods for advancing fronts. *J. Comput. Phys.* 169, 503–555.
- Sibarita, J.B., 2005. Deconvolution microscopy. *Adv. Biochem. Eng. Biot.* 95, 201–243.
- Simonoff, J.S., 1998. *Smoothing Method in Statistics*. Springer, New York.
- Stephens, D.J., Allan, V.J., 2003. Light microscopy techniques for live cell imaging. *Science* 300, 82–86.
- Sternberg, S.R., 1986. Grayscale morphology. *Comput. Vis. Graph.* 35, 333–355.
- Vincent, L., Soille, P., 1991. Watersheds in digital spaces—an efficient algorithm based on immersion simulations. *IEEE Pattern Anal.* 13, 583–598.